Sustainable Energy Technologies and Assessments 49 (2022) 101775

Contents lists available at ScienceDirect

Sustainable Energy Technologies and Assessments

journal homepage: www.elsevier.com/locate/seta

Original article

Rational design of $TiO_2/BiSbS_3$ heterojunction for efficient solar water splitting

Bhagatram Meena [a], Mohit Kumar [a], Sandeep Gupta [a], Lichchhavi Sinha [a], Palyam Subramanyam [b,*], Challapalli Subrahmanyam [a,*]

[a] Department of Chemistry, Indian Institute of Technology Hyderabad, Hyderabad, Telangana 502285, India
[b] Research Institute for Electronic Science, Hokkaido University, Sapporo, Hokkaido 001-0020, Japan

ARTICLE INFO

Keywords:
PEC water splitting
Charge separation
$BiSbS_3$
Chemical bath deposition
p-n junction

ABSTRACT

Solar induced water splitting with semiconductor photoelectrodes has been recognized as a sustainable alternative for addressing the energy crisis and pollution by creating hydrogen as a clean fuel. Insufficient light absorption and quick recombination of excitons are the most major bottlenecks in the emergence of semiconductor-based photocatalysts. The major challenge to the commercialization of this technique is the development of photoelectrodes that fulfill the PEC water-splitting requirements. In this study, As a photoanode for PEC water splitting, $BiSbS_3$ NRs were grown on TiO_2 films using a simple chemical bath deposition method. Such heterojunctions were chosen to amplify and expand the absorption of visible light, charge transport, charge separation and electrical conduction. The results show that the $TiO_2/BiSbS_3$ heterojunction photoanode exhibits relatively low charge transfer resistance, a highest current density of 5.0 $mA.cm^{-2}$ and STH conversion efficiency of 4.5% at 0.3 V vs RHE. The system's long-term stability was also evaluated for a period of 10,000 s and hydrogen evolution was carried out for 9000 s. Photoluminescence (PL) spectroscopy confirms that $TiO_2/BiSbS_3$ heterojunction exhibits stronger light absorption and efficient charge transfer compare to bare TiO_2 and $BiSbS_3$. Composite exhibits larger Brunauer – Emmett – Teller (BET) surface area compare to bare TiO_2 and $BiSbS_3$ which have contributed in excellent PEC performance compare to bare materials.

Introduction

The energy crisis, increasing pollution, and high fuel consumption have generated a paramount demand for clean, renewable, and sustainable energy sources that do not have harmful effects on the environment for future energy needs [1–5]. Photoelectrochemical (PEC) water splitting has evolved as a possible technology in recent decades to fulfill this demand because it converts sunlight into clean energy in the form of H_2 (hydrogen) [6–9]. In PEC devices, a semiconductor material with the appropriate bandgap and band positions for the oxidation/reduction potential of water is used as a photoelectrode to decompose H_2O into H_2 and O_2 by irradiating sunlight and applying an external bias [10–12]. Since the beginning of research on TiO_2-based photocatalysts by Fujishima and Honda in the early 1970s, photoanodes based on various metal oxides such as TiO_2, WO_3, Fe_2O_3, ZnO, and $BiVO_4$ have been used [13–17]. Among the metal oxides mentioned above, TiO_2 is mainly studied because of its advantages such as non-toxicity, natural resources, long-term photostability, and economic efficiency [18–20]. But it has wide bandgap (3.2 eV), so it can only consume ultraviolet light in the solar spectrum and has a limited solar-to-hydrogen (STH) efficiency owing to the quick charge recombination [21,22]. In order to strengthen the efficiency of TiO_2-based photoanodes, different approaches have been introduced, such as boosting the charge transfer by donor doping, minimising the surface charge recombination by catalyst aid or heterojunction construction, and altering the morphology of the nanoparticle [23–25]. In particular, p-n heterojunctions, in which two semiconductors with matching band positions are integrated, have been recognized as a promising technology for improving charge separation and transport [26–28]. Sensitization of TiO_2 and the formation of heterostructures to form type-II band alignment hetero-junctions has proven to be a successful strategy that leads to enhanced visible light absorption and boosts charge separation by increasing exciton lifetimes [29,30]. The staggered band gap alignment can promote an effective spatial separation of the photoinduced electrons and holes in these type-

* Corresponding authors.
E-mail addresses: subbu@es.hokudai.ac.jp (P. Subramanyam), csubbu@iith.ac.in (C. Subrahmanyam).

https://doi.org/10.1016/j.seta.2021.101775
Received 29 August 2021; Received in revised form 7 November 2021; Accepted 7 November 2021
Available online 19 November 2021

II band alignment heterostructures, where the edges of the valence and conduction bands are offset in both semiconductor moieties. As a result of the charge carriers being separated in the two independent moities, they have a longer lifetime and a lower rate of recombination [31]. Recently, metal chelcogenide based catalyst have gained much attention due to their exceptional optical properties and unique chemical and physical properties, among these group 15 binary chelcogineds of A_2X_3 and ternary chelcoginedes of ABX_3 have been used widely (whereas A, B = Bi, Sb, As and X = S, Se, Te) [32–34]. The integration of foreign ions into the crystal lattice of semiconductor nanocrystals can produce new functional properties. This concept has been adopted in the design of various energy materials for light harvesting, charge transport, and energy storage application. Upon Sb dilution into to Bi_2S_3 lattice, exciting new material properties, including induction of localized surface and a drastic change to the 1D crystal growth pattern. Recently, $BiSbS_3$, a p-type semiconductor, has been proved to be another catalyst for hydrogen generation by solar water splitting. $BiSbS_3$ has a narrow band gap of 1.6 eV and a relatively large absorption coeffiecient, it is commonly used to facilitate charge separation and broadens the absorption of the solar spectrum [35,36]. In case of band alignment, the semiconductors after the combination of appropriate p-n heterojunctions can be spatially separated by different electrodes due to the formation of an internal electric field in the space charge region by the interface of photoproduced charge carriers (e^--h^+) [37,38].

When the charge carriers generated by sunlight illumination are separated, electrons flow towards the counter electrode to increase the probability of reducing H^+ ion to H_2 (HER), and holes are supplied to trigger the oxygen evolution reaction (OER) at electrode/electrolyte surface [39,40]. Recently, In order to find out more, about the effect of heterojunction formation several investigations have been undertaken such as TiO_2/Bi_2S_3, TiO_2/Sb_2S_3, TiO_2/CdS, and $TiO_2/CuInS_2$ [41–44]. In particular, Freitas et al. reported TiO_2/Bi_2S_3 photoanode exhibited a current density of 0.3 mA.cm^{-2} at 0.3 V vs V_{SCE} (Ag/AgCl) and 0.44% STH at −0.5 V vs Ag/AgCl [45]. Chandra et al. recently reported TiO_2/Cu_2S photoanode demonstrating 13 mA.cm^{-2} at 0.6 V vs SCE [46]. Wang X. et al. reviewed a comprehensive study on TiO_2/In_2S_3 photoanode exhibited 1.8 mA.cm^{-2} at 1.0 V vs SCE [47]. Meena B. et al. reported a TiO_2/CdS nanomaterial-based photoanode showing a current density of 1.18 mA.cm^{-2} at 1.23 V vs RHE [43].

As a result of the aforementioned studies, we constructed a TiO_2/$BiSbS_3$ heterojunction and employ it as an efficient photoanode for solar water splitting. TiO_2/$BiSbS_3$ photoelectrode was fabricated by a doctor blade technique of TiO_2 followed by chemical bath deposition of $BiSbS_3$ on the conductive substrate as FTO. Fabricated photoanodes were examined for crystallinity, bandgap, and photoresponsivity by optical, physicochemical, and electrochemical studies. These results highlight the importance of heterojunctions due to the proper band arrangement of semiconductors. Hydrogen evolution was also carried out in alkaline condition at 1.23 V vs RHE. The plausible reaction mechanism of photocatalyst is discussed in detail.

Experimental section

Fabrication of TiO_2 / $BiSbS_3$ photoelectrode

The synthesis procedure of $BiSbS_3$ and TiO_2 photoelectrodes are given in supporting information (SI). $BiSbS_3$ was deposited on TiO_2 photoelectrode by the CBD method. To deposit $BiSbS_3$ thin film on TiO_2 photoelectrode, a solution of bismuth chloride (0.1 M) in DMSO and antimony chloride (0.1 M) in acetone was mixed in a beaker and sonicated for 5 min. Then thioacetamide (0.1 M) in acetone was mixed with the above mixture. The resulting mixture was stirred for 4 h and became a transparent solution. A fixed area of TiO_2 film was kept in the beaker containing the transparent solution for 24 h. After the end of the deposition period, a thin film was obtained. The thin film was removed from the bath, dried, and it was annealed at a temprature of 300 °C for half an hour in the presence of argon gas. The TiO_2 / $BiSbS_3$ photoanodes thin films turned colour from orange to a blackish brown. The schematic diagram of the fabricated electrodes is shown in Scheme1.

Results and discussion

The UV–Vis optical absorption spectra of the bare $BiSbS_3$ and TiO_2/$BiSbS_3$ are performed in 350 to 900 nm wavelength range and represented in Fig. 1. In the supporting information (SI), the absorption spectrum of TiO_2 is shown (SI) TiO_2 has an absorption edge at 390 nm (Fig. S1). The bare $BiSbS_3$ showed a broad absorption spectrum at 690 nm. On the other hand, the absorption spectrum of TiO_2/$BiSbS_3$ shows a red shift in wavelength at 750 nm compared to TiO_2 and pure $BiSbS_3$ which suggests that the integration of TiO_2 with $BiSbS_3$ to form TiO_2/$BiSbS_3$ composite could extend the absorbance edge in the visible spectra.

To understand the charge carrier transfer mechanism between $BiSbS_3$ and TiO_2/$BiSbS_3$ the fluorescence spectra were recorded. TiO_2/$BiSbS_3$ exhibits lower PL intensity at 825 nm which indicates the less feasibility of charge carrier recombination which is presented in Fig. 1b. In addition, the time-resolved photoluminescence (TRPL) were measured and presented in Fig. 1c, where the $BiSbS_3$ showed much longer average TRPL lifetime than TiO_2/$BiSbS_3$, which further proved the efficient charge transfer between TiO_2 and $BiSbS_3$ [6,48].

In order to determine the phase purity and crystal structure of the prepared materials, X-ray Diffraction (XRD) analysis were conducted. A muffle furnace at 500 °C for 30 min was used to restore the crystalline nature of TiO_2 to its original form. TiO_2 in the anatase phase shows a better photocatalytic response than the amorphous phase due to the greater charge carrier transfer. XRD patterns of (a) TiO_2, (b) $BiSbS_3$, and (c) TiO_2/$BiSbS_3$ are displayed in Fig. 2. The XRD spectrum of TiO_2 shows the crystallinity with diffraction peaks at 25.34°, 37.87°,48.12°, 54.01°, 55.07°, 62.72°, and 68.81° correspond to the (101), (103), (004), (200), (105), (211) and (204) planes. The nanomaterial is of anatase phase with a body-centered tetragonal crystal structure (JCPDS File No-894921). Similarly, the characteristic diffraction peaks for $BiSbS_3$ (Fig. 2 (b)) shown at 11.12°, 15.68°, 22.35°, 24.94°, 28.93, 32.08°, 46.38°, and 49.05° are indexed as (101), (200), (202), (301), (112), (212), (020), and (610) planes, respectively, as per ICDS File No-617029. TiO_2/$BiSbS_3$ composite exhibits the expected diffraction peaks for both anatase-TiO_2 and $BiSbS_3$ as shown in Fig. 2(c). It should be noted that the composite has not shown peak shifting, which signifies the absence of structural stress, and it is composed of only TiO_2 and $BiSbS_3$. It is noticed that $BiSbS_3$ can maintain its own crystal form in the TiO_2/$BiSbS_3$ composite. The peak intensities of TiO_2/$BiSbS_3$ at about 25.25° increases, which can be attributed to the peak superposition of TiO_2 at 25.34° and $BiSbS_3$ at 24.94°. Based on the XRD results, we can conclude that the TiO_2/$BiSbS_3$ composite with TiO_2 and $BiSbS_3$ phases is formed [49,50].

In order to determine the chemical composition and surface electronic structure of TiO_2 and $BiSbS_3$, additional XPS measurements were carried out, as well. As shown in Fig. 3(a), the XPS survey scan revealed the presence of Bi, Sb, S, Ti, and O elements in the composite. The binding energy (BE) positions were normalized to the C 1 s peak at 284.6 eV as shown in Fig. S2. Fig. 3(b) depicts two separate peaks with a spin-orbital splitting of 5.74 eV at binding energies of 458.36 eV and 464.1 eV, respectively, which correspond to the Ti $2P_{3/2}$ and Ti $2P_{1/2}$ in TiO_2/$BiSbS_3$. These peaks are symmetrical and consistent with Ti^{4+} in TiO_2 and complimented well with the earlier reported literature [51]. Fig. 3(c) shows the O 1 s spectrum of TiO2 at 529.6 eV, which corresponds to lattice oxygen (Ti-O-Ti). The Bi 4F XPS spectra of $BiSbS_3$ is shown in Fig. 3(d) with a binding energy of 157.5 and 163.5 eV, it is further deconvoluted into Bi $4F_{7/2}$ and Bi $4F_{5/2}$. The deconvoluted Sb $3d_{5/2}$ and Sb $3d_{3/2}$, peaks of $BiSbS_3$ (Fig. 3(e)) emerged at 530.3 and 541.7 eV BE, respectively. The presence of S $2P_{3/2}$ and S $2P_{1/2}$ is demonstrated by the peak splitting of the S 2P characteristic peaks at

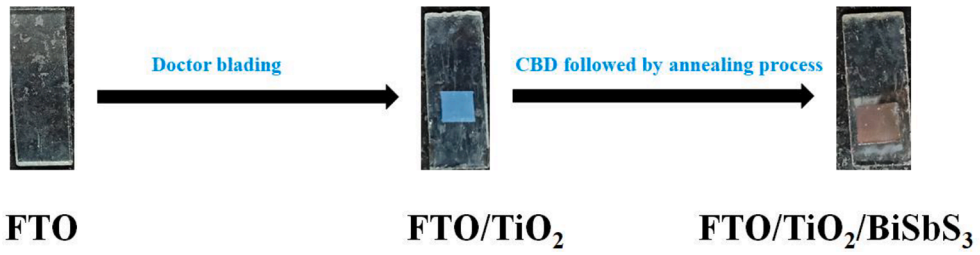

Scheme 1. Fabrication of FTO/TiO_2/$BiSbS_3$ photoelectrode.

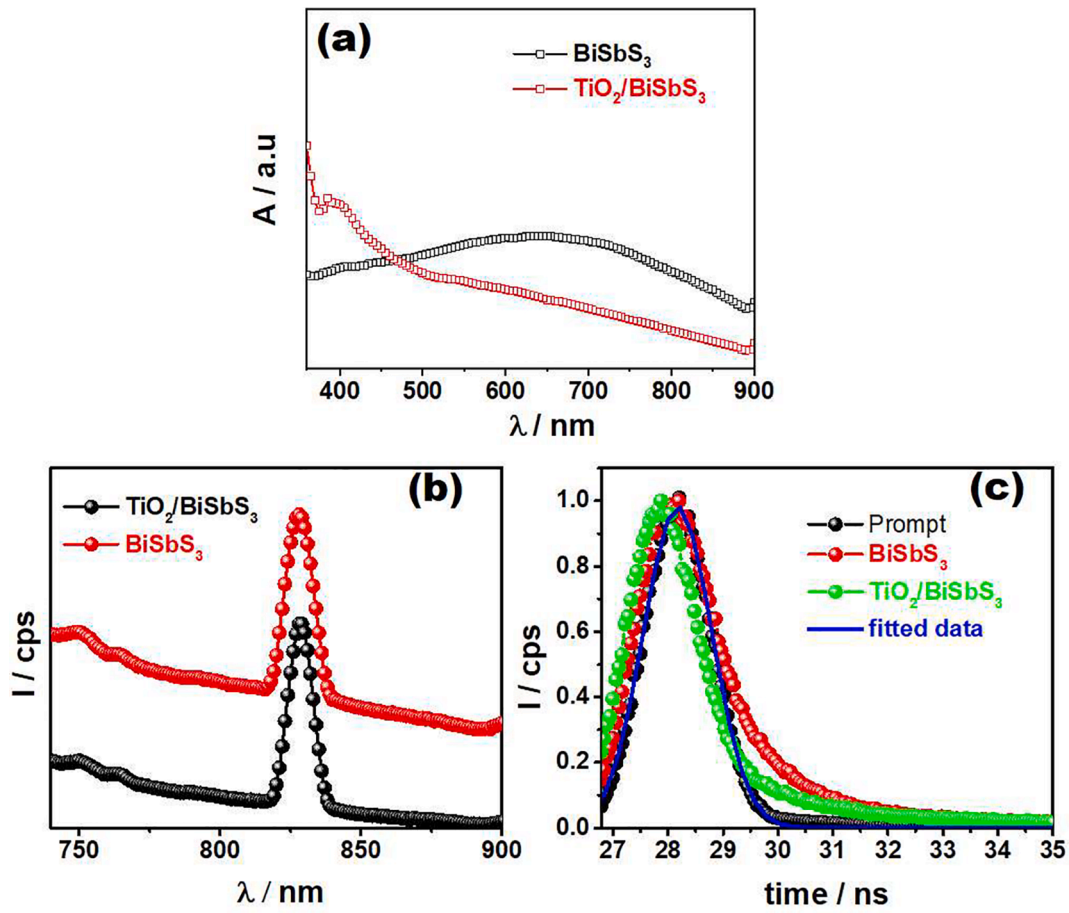

Fig. 1. (a) UV–Visible absorption spectra of bare $BiSbS_3$ and TiO_2 /$BiSbS_3$ composite (b) fluorescence spectra and (c) emission decay.

160.3 and 162.2 eV in Fig. 3(f). Each peak in the TiO_2/$BiSbS_3$ composite broad XPS spectrum correlates to a BE, as well. These results suggest the formation of a heterojunction. XPS spectra of bare TiO_2 and $BiSbS_3$ have been given in Figs. S6 and S7.

The morphology and microstrctural formation of the as prepared samples are analyzed by FESEM. Fig. 4a shows the uniformly formed irregular TiO_2 nanoparticles of different sizes. Fig. 4b depicts the formation of $BiSbS_3$ nanorods. The images shown in Fig. 4c shows the formation of the hybrid TiO_2 and $BiSbS_3$. It can be observed from the figure that the $BiSbS_3$ nanorods is evenly distributed over the TiO_2 nanoparticle as shown in inset. Additionally Fig. 4c also suggests the formation of agglomerated and attached $BiSbS_3$ nanorods together with the irregular and random TiO_2 nanoparticles. This heterostructure works as a conducting layer indicating strong interaction between both the nanomaterials. This will enhance the charge carrier transfer kinetics and their recombination. The EDS spectra has been taken for the hybrid material as shown in Fig. 4d to investigate the chemical composition. Furthermore, the EDS pattern it is concluded that all the elements are present in the material, confirming the existence of TiO_2/$BiSbS_3$ hetreostructure. The elemental mapping of the hybrid sample is given in Fig. 4(e–h). The map of the EDS characterization from the SEM image of the sample clearly reflects the homogenous distribution of the Ti, O, Bi, Sb, and S elements in the formed hybrid material.

Transmission electron microscope (TEM) experiments were conducted to study the morphologies, crystallinity, dimensions, and to obtain an insight into the scattering of TiO_2 and $BiSbS_3$ in the composite. Fig. 5(a) displays the TEM image of $BiSbS_3$ which shows the formation of agglomerated nanorods highlighted by dotted lines. Nanorods have an average length and diameter of 960 and 192 nm, whereas TiO_2 NPs have an average length and diameter of 25–35 nm and 65–70 nm respectively. The TEM image of TiO_2/$BiSbS_3$ composite is shown in Fig. 5(b) and it is observed that the $BiSbS_3$ NRs are uniformly distributed over TiO_2 nanoparticles. In addition, lattice fringes of TiO_2 and $BiSbS_3$ in composite are in good agreement with XRD data as dipcited in Fig. 5(c–d). This provides deep insight information to analyze the structure and morphology of the compound.

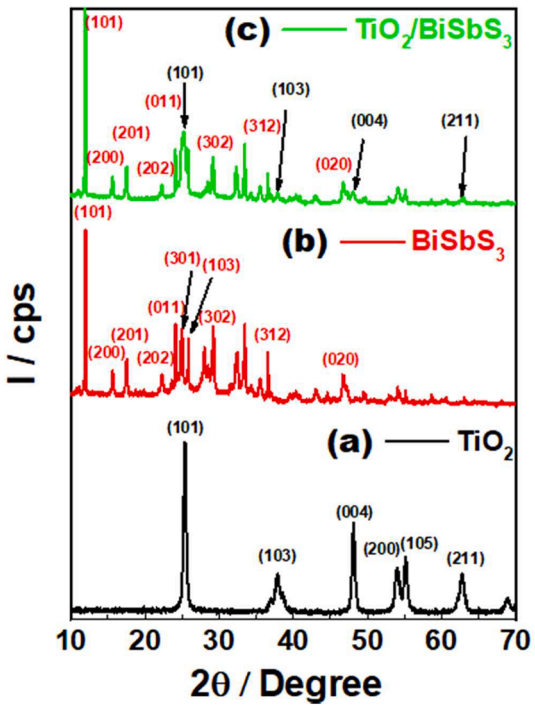

Fig. 2. XRD patterns of samples (a) TiO_2 (b) $BiSbS_3$ and (c) TiO_2 / $BiSbS_3$.

PEC studies

The PEC performance of photoanodes in an electrochemical cell was measured using a three-electrode system. The TiO_2, $BiSbS_3$, and TiO_2/$BiSbS_3$ materials were used as working electrodes (WE), a standard calomel electrode (Ag/AgCl) as a reference electrode (RE), and platinum wire as a counter electrode (CE). The performance was evaluated in a neutral electrolyte (Na_2SO_4, pH ~ 7) and aqueous alkaline electrolyte (Na_2S + Na_2SO_3, pH ~ 12.7) under chopped conditions.

Photoactivity of fabricated electrodes in the neutral electrolyte

Fig. 6(a) shows the linear sweep voltammetry curve of all three fabricated electrodes, i.e., TiO_2, $BiSbS_3$, and TiO_2/$BiSbS_3$ in the neutral condition. It is evident from the figure that the TiO_2/$BiSbS_3$ composite photoelectrode shows a photocurrent of 1.30 $mA.cm^{-2}$ at 1.23 V vs RHE, that is higher than TiO_2 and $BiSbS_3$ photoelectrode showing photocurrent density of 0.05 $mA.cm^{-2}$ and 0.2 $mA.cm^{-2}$. The photocurrent exhibited by the composite is 26 times higher than bare TiO_2 and 6.5 times higher than the pristine $BiSbS_3$ electrode. $BiSbS_3$ is a p-type semiconductor exhibiting dominating cathodic current. In this case, current densities are measured as anodic current and cathodic current to support the obtained results. LSV for bare $BiSbS_3$ photoelectrode is given in supplementary information (Fig. S4). In the absence of light, TiO_2, $BiSbS_3$, and TiO_2/$BiSbS_3$ electrodes show close to zero photocurrent but under light irradiation, the composite electrode shows a significant current, validating the efficiency of the composite material (TiO_2/$BiSbS_3$) for photoactivity. TiO_2 is a wide bandgap material, it can only absorb spectra in the UV region. In the case of composite material, there is a high photocurrent and due to the formation of TiO_2 heterojunction with $BiSbS_3$ charge separation phenomenon occurs [51]. On the other hand, $BiSbS_3$ is a narrow bandgap semiconductor, the recombination of the photoinduced charge carriers is faster, and thus the photoresponse is lower than desired [39]. The higher photocurrent response of TiO_2/$BiSbS_3$ is due to the greatly enhanced light absorption in the visible light region which facilitates the photoinduced charge carrier separation and transport. The composite photoanode also exhibits lower onset potential as compared to other photoelectrodes, which represents the OER kinetics at the electrode/electrolyte interface. The STH conversion efficiency in neutral condition has been calculated and shown in Fig. 6(b) using Eq. (1) [53,54].

$$STH(n\%) = J(1.23 - Vapp)/P \quad (1)$$

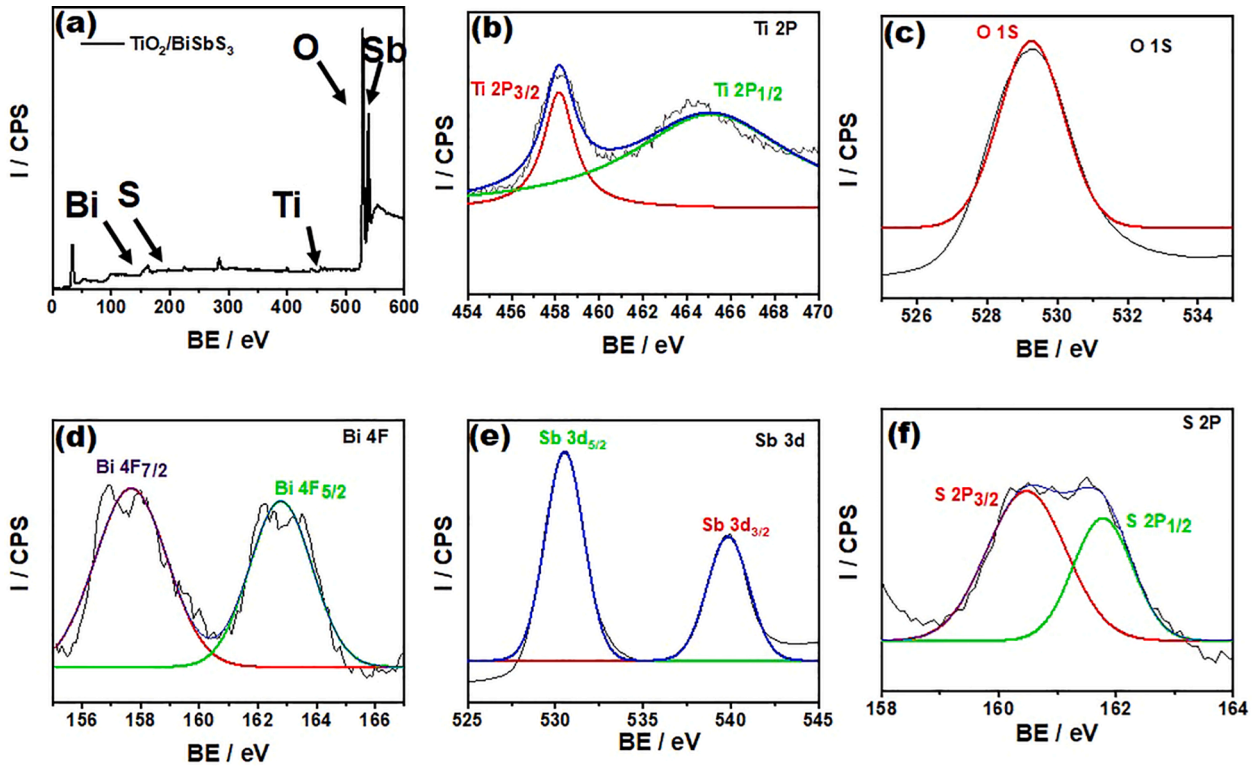

Fig. 3. XPS spectra for (a) survey scan of TiO_2/$BiSbS_3$ (b) Ti 2P (c) O 1S (d) Bi 4F (e) Sb 3d and (f) S 2P.

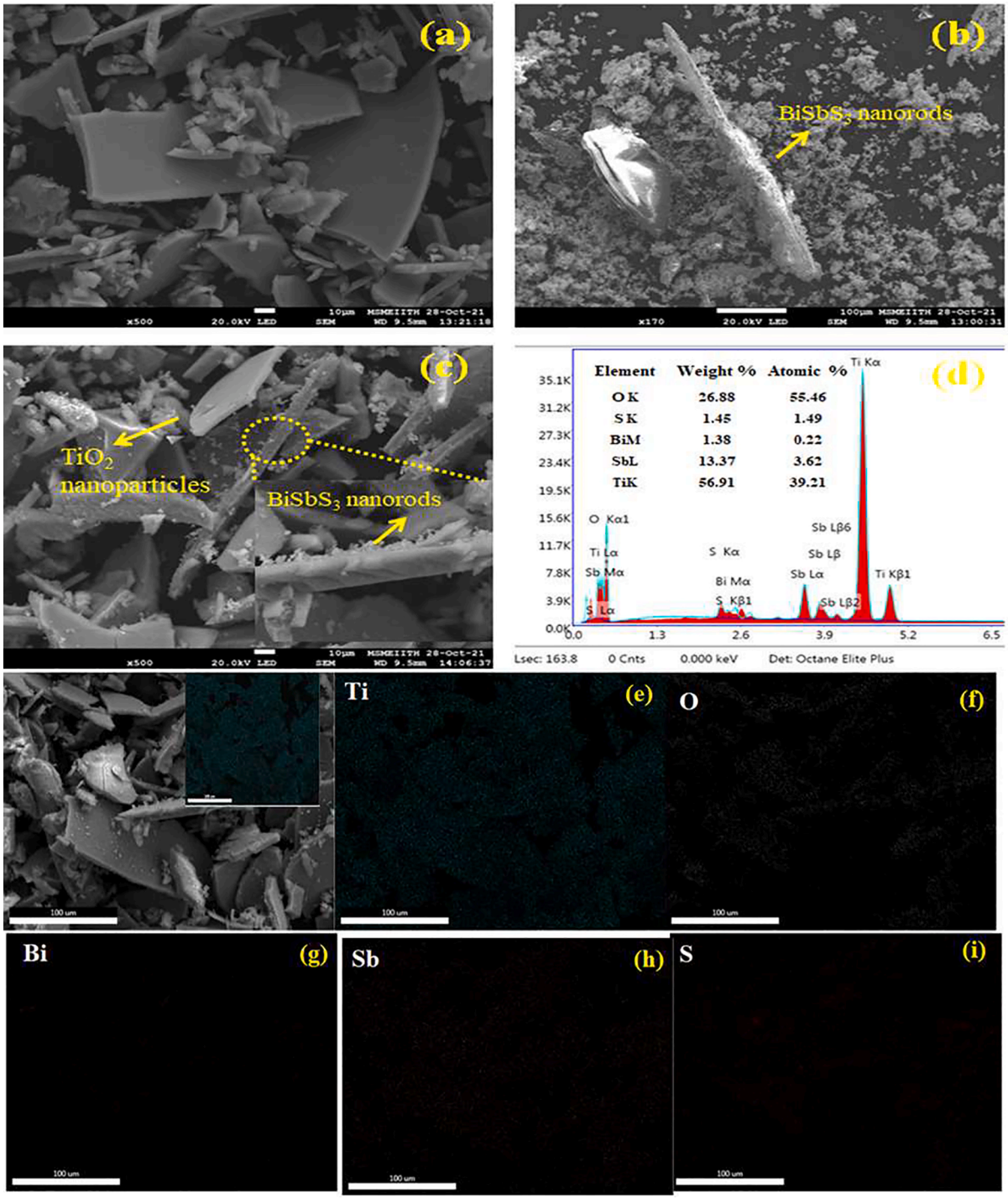

Fig. 4. SEM image of the (a) TiO_2 nanoparticles (b) $BiSbS_3$ nanorods (c) $TiO_2/BiSbS_3$ heterostructure (d) EDS spectra of the $TiO_2/BiSbS_3$ heterostructure and elemental mapping of the SEM image showing formation of (e) Ti (f) O (g) Bi (h) Sb and (i) S of $TiO_2/BiSbS_3$ heterostructure.

where, J, V, and P_{light}, are photocurrent density at the applied bias, applied potential versus RHE and the illumination intensity (100 mW cm^{-2}) respectively.

The composite electrode $TiO_2/BiSbS_3$ shows an STH conversion efficiency of 1.01% at 0.46 V which is greater than TiO_2 and $BiSbS_3$ providing efficiency of 0.02% and 0.06% indicating that the $TiO_2/BiSbS_3$ photoanode has a better carrier separation and transportation.

Photoactivity of fabricated electrodes in alkaline medium

Fig. 6(c) shows the LSV curve of the electrodes TiO_2, $BiSbS_3$, and $TiO_2/BiSbS_3$ in an alkaline medium. The composite material providing the photocurrent density of 5.0 mA.cm^{-2} is 25 times higher than bare TiO_2 and 6.5 times higher than $BiSbS_3$ giving a current density of 0.2 mA.cm^{-2} and 0.8 mA.cm^{-2} respectively. Here also, the current is almost negligible in the dark, but excellent photocurrent is obtained under light irradiation. The composite photoanode shows a negative shift in onset potential as compared to bare TiO_2 and $BiSbS_3$ due to the enhanced generation and separation of charge carriers. STH conversion

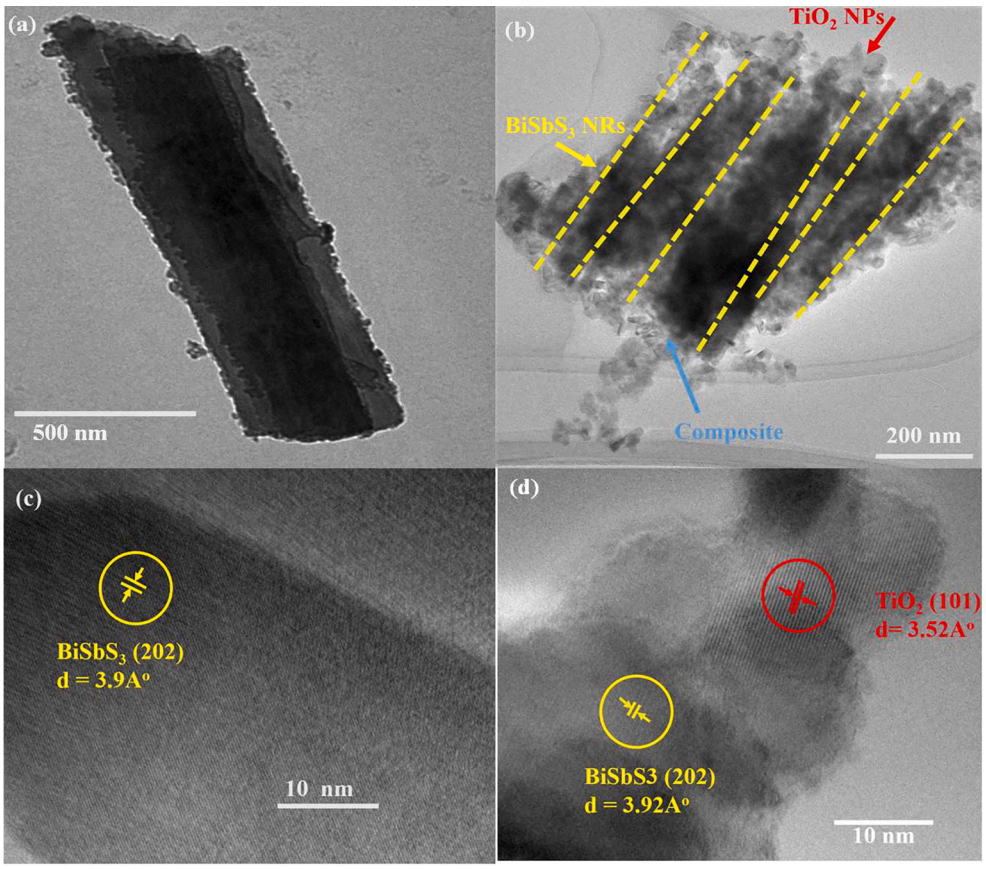

Fig. 5. HRTEM Image of (a) $BiSbS_3$-NRs and (b) TiO_2/$BiSbS_3$ NRs (c) lattice fringes of $BiSbS_3$ and (d) lattice fringes of TiO_2/$BiSbS_3$.

efficiencies of all three electrodes are calculated using equation (1) and plotted in Fig. 6(d). It is calculated as 0.1%, 0.35%, and 4.5% at 0.45 V vs RHE for TiO_2, $BiSbS_3$, and TiO_2/$BiSbS_3$ photoanodes respectively. The hole scavenging property of the electrolyte is the reason for the improved current and efficiency. Due to the hole scavenging property of the electrolyte, the recombination of the generated charge carriers is suppressed, and hydrogen can be produced efficiently at the Pt electrode. Hole scavengers allow reactions such as S^{-2}/S_2^{2-} and $SO_3^{2-}/S_2O_3^{2-}$ in the alkaline electrolytes [52].

To confirm the stability of the photoelectrode of TiO_2, $BiSbS_3$ and TiO_2/$BiSbS_3$, chronoamperometry was performed in an alkaline medium at 1.23 V vs RHE under the light illumination condition. The photocurrent value is almost consistent with the acquired LSV value. Fig. 7a displayed the TiO_2/$BiSbS_3$ exhibited significant stability over 10000 s with almost no decay, whereas TiO_2 and $BiSbS_3$ exhibited lower current densities. This indicates the stability of the composited material in the alkaline medium due to the mechanism of feasible charge transfer, proper band alignment, and hole scavengers capturing hole charge carriers and suppressing recombination [45]. This phenomenon helps the photoinduced electronic charge carriers to reach the counter electrode at a fixed time interval without compromising the stability. TiO_2/$BiSbS_3$ photostability was carried out for almost 10 h and its shows no decay that can be seen in Fig S8.

Electrochemical impedance spectroscopy (EIS) measurments were carried out at an open-circuit potential 1.23 V vs RHE in the applied frequency window of 1 MHz to 10^{-1} Hz under continuous light irradiation to further confirm the charge transfer rate and recombination on the WE/electrolyte interface. As it can be seen in inset of Fig. 7b, a Randles circuit was designed employing Nyquist plots, which aids in determining the charge transfer resistance (R_{CT}). Table 1 of the supporting information lists the fitted parameters. The R_{CT} values for TiO_2, $BiSbS_3$, and TiO_2/$BiSbS_3$ photoanodes, respectively, are 9110, 854, and 276. The composite has a lower R_{CT} than the other photoanodes, and the fact that TiO_2/$BiSbS_3$ has a low R_{CT} indicates that charge separation and transportation are subtle. Fig. 7b reveals that the composite electrode has a smaller semicircular area compare to bare TiO_2 and $BiSbS_3$, indicating that the composite electrode has a better charge transfer capability [55]. Additionally, the phase angle shifts to low frequency and the resistance lowers at different frequencies in the Bode plots of TiO_2, $BiSbS_3$ and TiO_2/$BiSbS_3$ photoanodes, showing that proper band alignment of TiO_2 and $BiSbS_3$ combined can significantly promote a fast charge transfer (Fig. S5) [58].

Mott-schottky experiments were carried out to identify the nature of fabricated photoanodes TiO_2, $BiSbS_3$ and TiO_2/$BiSbS_3$.The negative slope of $BiSbS_3$ indicates that it is a p-type semiconductor and positive slope of the TiO_2 indicates that it is an n-type semiconductor whereas TiO_2/$BiSbS_3$ shows V-shape curves that indicates the formation of p-n junction [56,59,60]. The Mott-Schottky plots for the electrodes are shown in Fig. 8a–c. The hydrogen evolution activity of TiO_2/$BiSbS_3$ photoelectrode was performed as a function of time at 1.23 V vs RHE in aqueous electrolyte of 0.1 M Na_2S + 0.1 M Na_2SO_3 and result is displayed in the Fig. 8d. During the 2.5 h period, the hydrogen evolution of the TiO_2/$BiSbS_3$ photoanode was 2.14, 4.33, 6.71, 7.16 and 9.81 μmol respectively. The higher hydrogen evolution for TiO_2/$BiSbS_3$ could be attributed to proper band alignment of TiO_2 and $BiSbS_3$.

Plausible mechanism

The plausible charge transfer mechanism has been shown below in Fig. 9. A space charge layer will form at the interface between the n-type and p-type semiconductor layer in heterojunction systems. The formation of space charge layer takes place due to the movement of majority charge carriers from p-type to n-type semiconductor. It leads to the evolution of p-n junction and the generation of an electric field at the

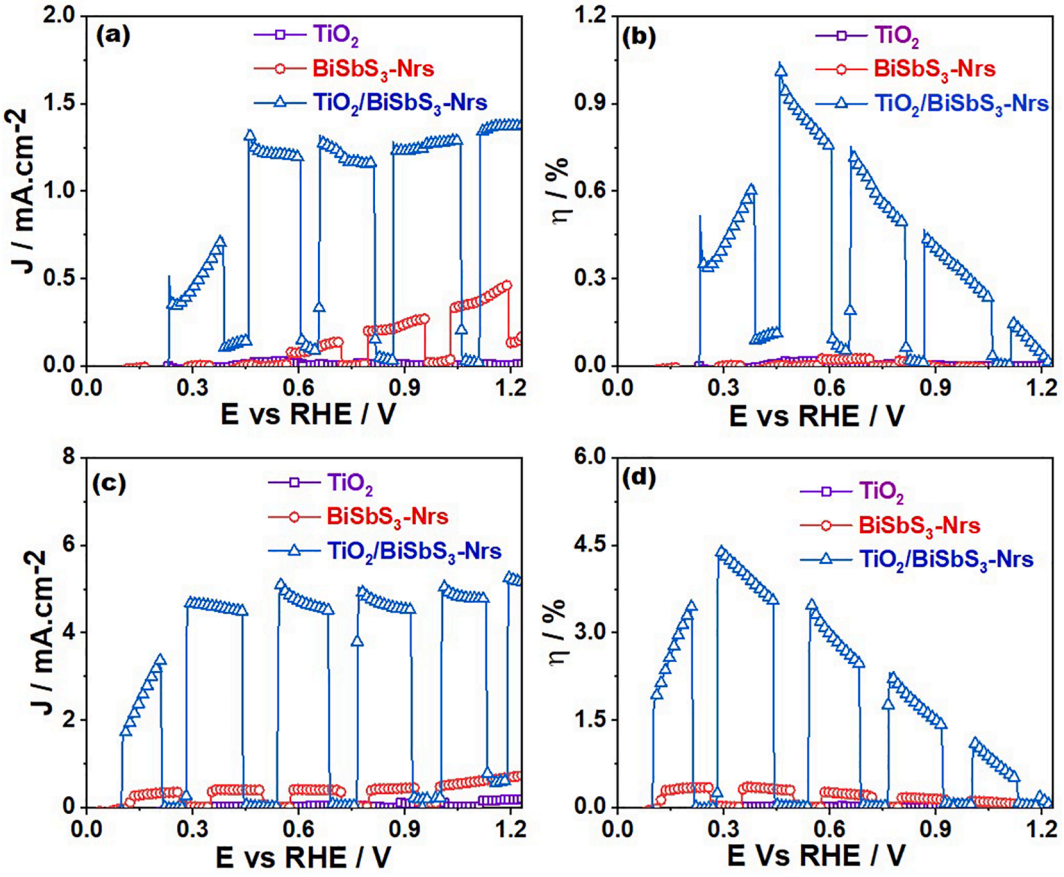

Fig. 6. Linear sweep voltammetry curves and Solar to hydrogen efficiency plot for TiO_2, $BiSbS_3$ and $TiO_2/BiSbS_3$ photoanodes (a&b) in neutral condition, (c&d) in alkaline conditions.

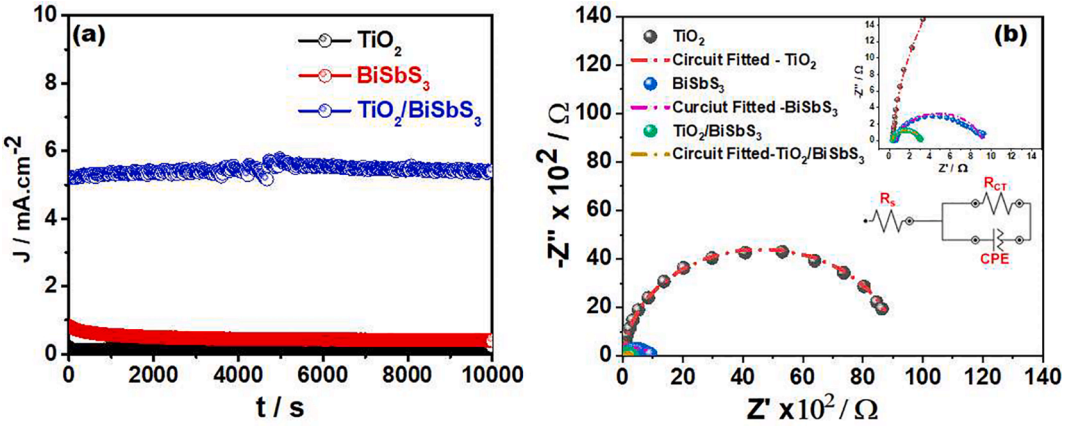

Fig. 7. (a) Stability plots and (b) Nyquist plots of TiO_2, $BiSbS_3$ and $TiO_2/BiSbS_3$ photoanodes.

junction of the semiconductors [57]. In type II heterojunction system charge transfer process depends on conduction band (CB), valancy band (VB) and fermi level positions. To calculate the conduction band position of TiO_2 and $BiSbS_3$, cyclic voltammetry (CV) measurement was carried out and results are plotted in Fig. S9a and S9b. The optical bandgap of TiO_2 is 3.17 eV while calculated CB and VB positions are at −0.46 V and 2.71 V vs RHE respectively. The bandgap for $BiSbS_3$ is 1.8 eV with CB and VB positioning at −1.2 and 0.6 V vs RHE respectively. Simultaneously construction of $TiO_2/BiSbS_3$ heterojunction is formed, the Fermi energy levels will alter and reach a state of alignment movement of majority charge carriers from each of the semiconductors. A space charge layer, internal electric field and bending of energy bands are being generated at the $TiO_2/BiSbS_3$ interface. Upon light illumination of $TiO_2/BiSbS_3$, the photoproduced electrons from the CB of $BiSbS_3$ are transferred to the CB of TiO_2 which facilitate the HER at counter electrode moreover photoproduced holes are moved from the VB of TiO_2 to the VB of $BiSbS_3$ which gives the OER at the electrode/electrolyte surface [61]. The electric field generated at the interfacial sites between TiO_2 and $BiSbS_3$ facilitates the transporatation of charge carriers resulting in the enhancement of the charge separation and suppression of charge recombination. Efficient charge plays an important role in achieving the photocurrent density of $TiO_2/BiSbS_3$ higher than that of

Table 1
Comparison of other reported TiO_2 based heterojunction and there PEC water splitting properties.

Sr. No.	Electrode materials	Current density ($mAcm^{-2}$)	Electrolyte	Synthesis Method	References (Publishing Year)
1	TiO_2/PbS	3	Polysulfide	Silar Method	[1], 2021
2	TiO_2/CdS	2.03	0.3 M Na_2SO_3 + 0.25 M Na_2S	CBD	[2], 2019
3	TiO_2/Sb_2S_3/rGo	0.039	0.1 M Na_2SO_4	One pot synthesis	[3], 2021
4	TiO_2/Bi_2S_3	3.98	0.1 M Na_2S + Na_2SO_3	Hydrothermal	[4], 2021
5	TiO_2/Bi_2S_3	1.76	0.1 M Na_2S + Na_2SO_3	Hydrothermal	[6], 2021
6	TiO_2/Bi_2Se3	0.8	0.1 M Na_2SO_4	Hydrothermal	[6], 2021
7	TiO_2/In_2S_3/CdS	0.18	0.25 M Na_2S + 0.35 m Na_2SO_3	Hydrothermal	[5], 2016
8	TiO_2/Ag_2Se	0.4	0.1 M Na_2S + Na_2SO_3	Hydrothermal	[43], 2021
9	TiO_2/CuS	0.015	0.1 M Na_2SO_4	Solution based process	[46], 2018
10	**TiO_2/$BiSbS_3$**	**5.0**	**0.1 M Na_2SO_3 + 0.1 M Na_2S**	**CBD**	**Our Work**

TiO_2 and $BiSbS_3$ photoanodes.

Conclusion

The CBD method was used to make $TiO_2/BiSbS_3$ nanocomposite, which was then used as photoanodes for photoelectrochemical water splitting. The prepared $TiO_2/BiSbS_3$ nanocomposite photoanode showed improved visible light photoresponse and better PEC performance. $TiO_2/BiSbS_3$ nanocomposite photoanode exhibited higher photocurrent density of 1.3 $mA.cm^{-2}$ at 1.23 V vs RHE and high STH conversion efficiencies (1.01% at 0.46 V vs RHE) as respect to the TiO_2 and $BiSbS_3$ in neutral medium. The $TiO_2/BiSbS_3$ nanocomposite photoanode has a 5 times higher photocurrent density of 5 $mA.cm^{-2}$ at 1.23 V vs RHE and a 4.5% STH conversion efficiency in alkaline medium than TiO_2 due to the influence of hole scavengers. The composite has low charge recombination, according to EIS. The easy transit of photogenerated electrons from CB of $BiSbS_3$ to CB of TiO_2, that also reduces charge recombination, is responsible for the improved PEC performance. PEC performance for hydrogen production is possible with this new binary electrode. Photoluminescence (PL) spectroscopy experiment confirms that $TiO_2/BiSbS_3$ heterojunction exhibits stronger light absorption and efficient charge transfer compare to bare TiO_2 and $BiSbS_3$. Composite produced larger Brunauer – Emmett – Teller (BET) surface area compare to bare TiO_2 and $BiSbS_3$ which have contributed in excellent PEC performance compare to bare materials.

Credit authorship contribution statement

Bhagatram Meena: is the first author, He planned to design the scheme, conducted the work and finally wrote the manuscript. Mohit Kumar: helped in the characterization and fabrications of samples. Sandeep Gupta: helped to characterize the fabri-cated samples. Lichchhavi Sinha: helped in literature review, correcting the typo errors and english grammar of the manuscript. Challapalli Subrahmanyam: is the corresponding author, He helped in designing the work and wrote the manuscript. Palyam Subramanyam: is the corresponding author, He helped in designing the work and wrote the manuscript.

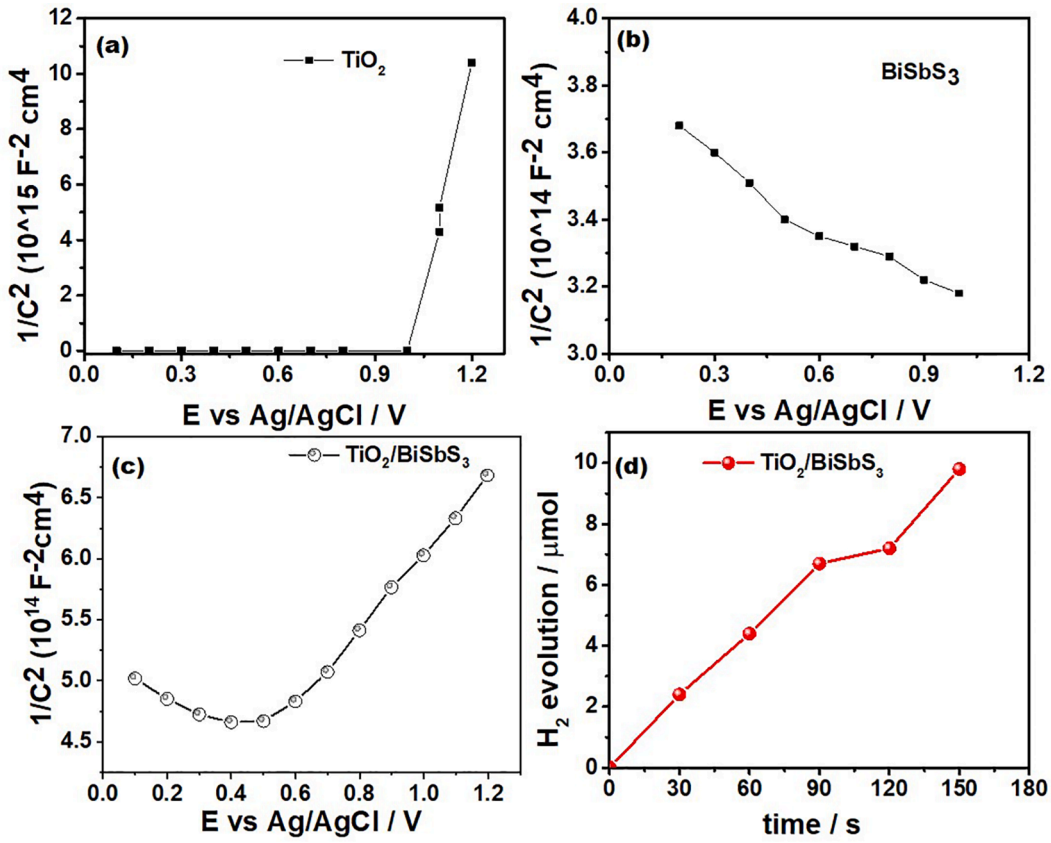

Fig. 8. Mott-schottky plot of (a) TiO_2 (b) $BiSbS_3$ (c) $TiO_2/BiSbS_3$ and (d) Hydrogen quantification.

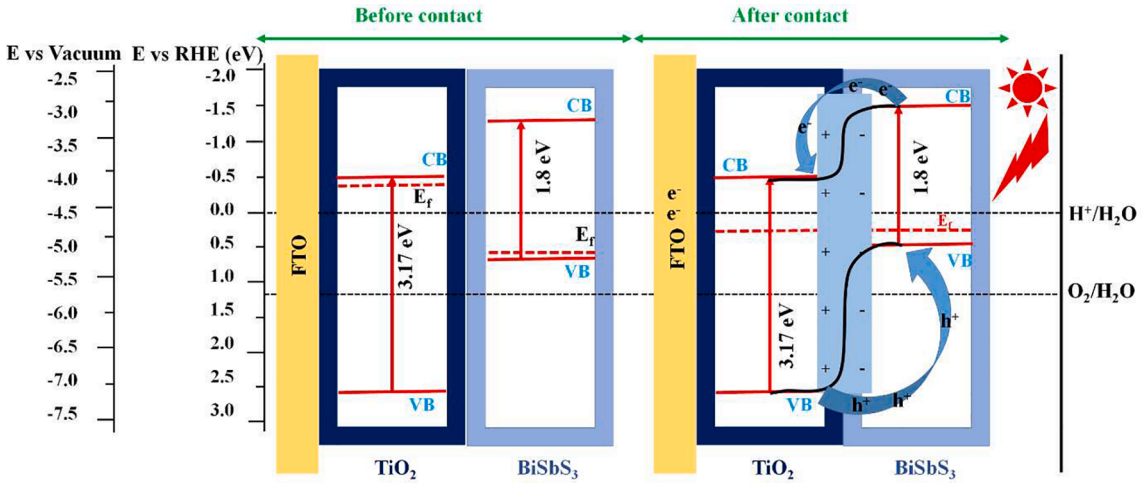

Fig. 9. Plausible charge transfer mechanism of $TiO_2/BiSbS_3$ photoanode.

Declaration of Competing Interest

The authors declare that they have no known competing financial interests or personal relationships that could have appeared to influence the work reported in this paper.

Acknowledgement

B. R. M. and M. K. are grateful for the CSIR research fellowship India.

Appendix A. Supplementary data

Supplementary data to this article can be found online at https://doi.org/10.1016/j.seta.2021.101775.

References

[1] Bak T, Nowotny J, Rekas M, Sorrell CC. Photo-electrochemical hydrogen generation from water using solar energy. Materials-related aspects. Int J Hydrog Energy 2002;27:991–1022.
[2] Wang XC, Maeda K, Chen XF, Takanabe K, Domen K, Hou YD, et al. Polymer Semiconductors for Artificial Photosynthesis: Hydrogen Evolution by Mesoporous Graphitic Carbon Nitride with Visible Light. J Am Chem Soc 2009;131:1680–1.
[3] Dresselhaus MS, Thomas IL. Alternative energy technologies. Nature 2001;414:332–7.
[4] Stambouli AB, Traversa E. Fuel cells, an alternative to standard sources of energy. Renew Sust Energy Rev 2002;6:295–304.
[5] Walter MG, Warren EL, McKone JR, Boettcher SW, Mi Q, Santori EA, et al. Water Splitting Cells. Chem Rev 2010,110,:6446–73.
[6] Subramanyam P, Meena B, Suryakala D, Subrahmanyam C. TiO_2 Photoanodes Sensitized with Bi_2Se_3 Nanoflowers for Visible–Near-Infrared Photoelectrochemical Water Splitting. ACS Appl Nano Mater 2021;4:739–45.
[7] Sheppard LR, Wuhrer R. TiO_2-Based homojunction photo-electrode for solar-driven water splitting. Int J Hydrog Energy 2020;45:9386–96.
[8] Nowotny J, Bak T, Nowotny MK, Sheppard LR. TiO_2 surface active sites for water splitting. J Phys Chem B 2006;110:18492–5.
[9] Seabold JA, Shankar K, Wilke RHT, Paulose M, Varghese OK, Grimes CA, et al. Photoelectrochemical Properties of Heterojunction CdTe/TiO_2 Electrodes Constructed Using Highly Ordered TiO_2 Nanotube Arrays. Chem Mater 2008;20:5266–73.
[10] Hisatomi T, Kubota J, Domen K. Recent Advances in Semiconductors for Photocatalytic and Photoelectrochemical Water Splitting. Chem Soc Rev 2014;43:7520–35.
[11] Subramanyam P, Vinodkumar T, Deepa M, Subrahmanyam C. Gold nanoparticle decorated bismuth sulfide nanorods for enhanced photoelectrochemical hydrogen production. J Mater Chem C 2019;7:6398–405.
[12] Cao S-W, Yuan Y-P, Fang J, Shahjamali MM, Boey FYC, Barber J, et al. In-Situ Growth of CdS Quantum Dots on g-C_3N_4 Nanosheets for Highly Efficient Photocatalytic Hydrogen Generation under Visible Light Irradiation. Int J Hydrog Energy 2013;38(3):1258–66.
[13] Fujishima Akira, Honda Kenichi. Electrochemical photolysis of water at a semiconductor electrode. Nature 1972;238(5358):37–8.
[14] Subramanyam P, Meena B, Sinha GN, Deepa M, Subrahmanyam C. Decoration of plasmonic Cu nanoparticles on WO_3/Bi_2S_3 QDs heterojunction for enhanced photoelectrochemical water splitting. Int J Hydrog Energy 2020;45:7706–15.
[15] Hu YS, Kleiman-Shwarsctein A, Forman AJ, Hazen D, Park JN, McFarland EW. Pt-doped α-Fe_2O_3 thin films active for photoelectrochemical water splitting. Chem Mater 2008;20:3803–5.
[16] Shao M, Ning F, Wei M, Evans DG, Duan X. Hierarchical nanowire arrays based on ZnO core– layered double hydroxide shell for largely enhanced photoelectrochemical water splitting. Adv Funct Mater 2014;24:580–6.
[17] Subramanyam P, Vinodkumar T, Nepak D, Deepa M, Subrahmanyam C. Mo-doped $BiVO_4$@ reduced graphene oxide composite as an efficient photoanode for photoelectrochemical water splitting. Catal Today 2019;325:73–80.
[18] Subramanyam P, Deepa M, Raavi SSK, Misawa H, Biju V, Subrahmanyam C. A photoanode with plasmonic nanoparticles of earth abundant bismuth for photoelectrochemical reactions. Nanoscale Adv 2020;2:5591–9.
[19] Zhang Z, Wang P. Optimization of photoelectrochemical water splitting performance on hierarchical TiO_2 nanotube arrays. Energy Environ Sci 2012;5:6506–12.
[20] Zhan Z, An J, Zhang H, Hansen RV, Zheng L. Three-dimensional plasmonic photoanodes based on Au-embedded TiO_2 structures for enhanced visible-light water splitting. ACS Appl Mater Interfaces 2014;6:1139–44.
[21] Rodríguez-Hernández F, Tranca DC, Martínez-Mesa A, Uranga-Piña L, Seifert G. Water splitting on transition metal active sites at TiO_2-based electrodes: a small cluster study. J Phys Chem C 2016;120:25851–60.
[22] Boppella R, Kochuveedu ST, Kim H, Jeong MJ, Marques Mota F, Park JH, et al. Plasmon-sensitized graphene/TiO_2 inverse opal nanostructures with enhanced charge collection efficiency for water splitting. ACS Appl Mater Interfaces 2017;9:7075–83.
[23] Liu Q, Lu H, Shi Z, Wu F, Guo J, Deng K, et al. 2D $ZnIn_2S_4$ nanosheet/1D TiO_2 nanorod heterostructure arrays for improved photoelectrochemical water splitting. ACS Appl Mater Interfaces 2014;6:17200–7.
[24] Feng W, Lin L, Li H, Chi B, Pu J, Li J. Hydrogenated TiO_2/ZnO heterojunction nanorod arrays with enhanced performance for photoelectrochemical water splitting. Int J Hydrog Energy 2017;42:3938–46.
[25] Zhou Tingsheng, Wang Jiachen, Chen Shuai, Bai Jing, Li Jinhua, Zhang Yan, et al. Bird-nest structured ZnO/TiO_2 as a direct Z-scheme photoanode with enhanced light harvesting and carriers kinetics for highly efficient and stable photoelectrochemical water splitting. Appl Catal B-Environ 2020;267:118599. https://doi.org/10.1016/j.apcatb.2020.118599.
[26] Niu M, Cao D, Sui K, Liu C. InP/TiO_2 heterojunction for photoelectrochemical water splitting under visible-light. Int J Hydrog Energy 2020;45:11615–24.
[27] Wang Y, Cao S, Huan Y, Nie T, Ji Z, Bai Z, et al. The effect of composite catalyst on Cu_2O/TiO_2 heterojunction photocathodes for efficient water splitting. Appl Surf Sci 2020;526:146700.
[28] Naceur JB, Ouertani R, Chakhari W, Chtourou R. Photo-electrochemical properties of Sb_2S_3/TiO_2 heterostructures integrally synthesis by hydrothermal method. J Mater Sci: Mater Electron 2019;30:5631–9.
[29] Khedr MH, Bahgat M, Rouby WE. Synthesis, magnetic properties and photocatalytic activity of $CuFe_2O_4/MgFe_2O_4$ and $MgFe_2O_4/CuFe_2O_4$ core/shell nanoparticles. Mater Technol 2008;23:27–32.
[30] Lin J, Liu Y, Liu Y, Huang C, Liu W, Mi X, et al. SnS_2 nanosheets/H-TiO_2 nanotube arrays as a type II heterojunctioned photoanode for photoelectrochemical water splitting. ChemSusChem 2019;12:961–7.
[31] Chen Shangrong, Li Changlin, Hou Zhongyu. A novel in situ synthesis of TiO_2/CdS heterojunction for improving photoelectrochemical water splitting. Int J Hydrog Energy 2019;44(47):25473–85.
[32] Zhang Hulin, Hu Chenguo, Ding Yong, Lin Yuan. Synthesis of 1D Sb_2S_3 nanostructures and its application in visible-light-driven photodegradation for MO. J Alloy Compd 2015;625:90–4.

[33] Song Yung-Tao, Lin Lu-Yin, Hong Jia-Yo. Enhanced visible-light response and conductivity of the TiO_2/reduced graphene oxide/Sb_2S_3 heterojunction for photoelectrochemical water oxidation. Electrochim Acta 2016;211:576–85.
[34] Li Y, Yang W, Wang C, Li Z, Lai J, Wang L, et al. Achieving Controllable $CoTiO_3$-Encapsulated TiO_2 Heterostructures for Enhanced Photoelectrochemical Water Splitting. ACS Appl Energy Mater 2019;2:8229–35.
[35] Patra BK, Khilari S, Bera A, Mehetor SK, Pradhan D, Pradhan N. Chemically filled and Au-coupled $BiSbS_3$ nanorod heterostructures for photoelectrocatalysis. Chem Mater 2017;29:1116–26.
[36] Wen S, Zhao J, Chen J, Yang J, Xu J. $BiSbS_3$@ N-doped carbon core–shell nanorods as efficient anode materials for sodium-ion batteries. Dalton Trans 2019;48:10448–54.
[37] Bai S, Liu J, Cui M, Luo R, He J, Chen A. Two-step electrodeposition to fabricate the p–n heterojunction of a $Cu_2O/BiVO_4$ photoanode for the enhancement of photoelectrochemical water splitting. Dalton Trans 2018;47:6763–71.
[38] Pan Q, Zhang C, Xiong Y, Mi Q, Li D, Zou L, et al. Boosting charge separation and transfer by plasmon-enhanced $MoS_2/BiVO_4$ p–n heterojunction composite for efficient photoelectrochemical water splitting. ACS Sustain Chem Eng 2018;6:6378–87.
[39] Subramanyam P, Meena B, Neeraja Sinha G, Suryakala D, Subrahmanyam C. Facile Synthesis and Photoelectrochemical Performance of a Bi_2S_3@rGO Nanocomposite Photoanode for Efficient Water Splitting. Energy Fuels 2021;35:6315–21.
[40] Subramanyam, P.; Meena, B.; Suryakala, D.; Deepa, M.; Subrahmanyam, C. Plasmonic nanometal decorated photoanodes for efficient photoelectrochemical water splitting. Catal Today (2020).
[41] Chen X, Zhang Z, Chi L, Nair AK, Shangguan W, Jiang Z. Recent advances in visible-light-driven photoelectrochemical water splitting: catalyst nanostructures and reaction systems. Nanomicro Lett 2016;8:1–12.
[42] Lu X, Liu Z, Zhao L. TiO_2 hierarchical porous films sensitized by Sb_2S_3 nanoparticles for enhanced photoelectrochemical properties. J Solgel Sci Technol 2017;82:157–66.
[43] Meena Bhagatram, Subramanyam Palyam, Suryakala Duvvuri, Biju Vasudevanpillai, Subrahmanyam Challapalli. Efficient solar water splitting using a CdS quantum dot decorated TiO_2/Ag_2Se photoanode. Int J Hydrog Energy 2021;46(69):34079–88.
[44] Guo K, Liu Z, Han J, Liu Z, Li Y, Wang B, et al. Hierarchical TiO_2.$CuInS_2$ core–shell nanoarrays for photoelectrochemical water splitting. PCCP 2014;16:16204–13.
[45] Freitas DV, González-Moya JR, Soares TA, Silva RR, Oliveira DM, Mansur HS, et al. Enhanced visible-light photoelectrochemical conversion on TiO_2 nanotubes with Bi_2S_3 quantum dots obtained by in situ electrochemical method. ACS Appl Energy Mater 2018;1:3636–45.
[46] Chandra M, Bhunia K, Pradhan D. Controlled synthesis of CuS/TiO_2 heterostructured nanocomposites for enhanced photocatalytic hydrogen generation through water splitting. Inorg Chem 2018;57:4524–33.
[47] Wang X, Li H, Zhang J, Liu X, Zhang X. Wedged ß-In_2S_3 sensitized TiO_2 films for enhanced photoelectrochemical hydrogen generation. J Alloy Compd 2020;831:154798.
[48] Li, L.; Gan, L.; Zhang, Z. Encapsulation Strategy on All Inorganic Perovskites for Stable and Efficient Photoelectrocatalytic Water Splitting. Adv. Mater. Interfaces 2021;2100202.
[49] Jiang, F.,; Yan, T.; Chen, H.; Sun, A.; Xu, C.; Wang, X. A g-C_3N_4–CdS composite catalyst with high visible-light-driven catalytic activity and photostability for methylene blue degradation. Appl Surf Sci 2014;295:164–72.
[50] Kumar KA, Chandana L, Ghosal P, Subrahmanyam C. Simultaneous photocatalytic degradation of p-cresol and Cr (VI) by metal oxides supported reduced graphene oxide. Mol Catal 2018;451:87–95.
[51] Wang Y, Zheng YZ, Lu S, Tao X, Che Y, Chen JF. Visible-light-responsive TiO_2-coated ZnO: I nanorod array films with enhanced photoelectrochemical and photocatalytic performance. ACS Appl Mater Interfaces 2015;7:6093–101.
[52] Quang ND, Hien TT, Chinh ND, Kim D, Kim C, Kim D. Transport of photo-generated electrons and holes in TiO_2/CdS/CdSe core-shell nanorod structure toward high performance photoelectrochemical cell electrode. Electrochim Acta 2019;295:710–8.
[53] Kim Young Been, Jung Sung Hyeon, Kim Dong Su, Deshpande Nishad G, Lee Ho Seong, Cho Hyung Koun. Interleaved biphasic p–n blended copper indium selenide photoelectrode and its application in pulse-driven photoelectrochemical water splitting. Appl Catal B-Environ 2021;285:119839. https://doi.org/10.1016/j.apcatb.2020.119839.
[54] Huang J, Liu T, Wang R, Zhang M, Wang L, She H, et al. Facile loading of cobalt oxide on bismuth vanadate: proved construction of pn junction for efficient photoelectrochemical water oxidation. J Colloid Interface Sci 2020;570:89–98.
[55] Wang Yinsi, Liang Yujie, Zeng Dong, Zhu Min, Fu Junli, Zhu Tianyu, et al. Electrochemical deposition of p-type β-$Ni(OH)_2$ nanosheets onto CdS nanorod array photoanode for enhanced photoelectrochemical water splitting. Electrochim Acta 2020;337:135763. https://doi.org/10.1016/j.electacta.2020.135763.
[56] Chen Y, Feng X, Liu Y, Guan X, Burda C, Guo L. Metal oxide-based tandem cells for self-biased photoelectrochemical water splitting. ACS Energy Lett 2020;5:844–66.
[57] Soltani T, Tayyebi A, Lee BK. $BiFeO_3/BiVO_4$ p– n heterojunction for efficient and stable photocatalytic and photoelectrochemical water splitting under visible-light irradiation. Catal Today 2020;340:188–96.
[58] Ye Sheng, Shi Wenwen, Liu Yong, Li Dongfeng, Yin Hang, Chi Haibo, et al. Unassisted Photoelectrochemical Cell with Multimediator Modulation for Solar Water Splitting Exceeding 4% Solar-to-Hydrogen Efficiency. **J** Am Chem Soc 2021;143(32):12499–508.
[59] Wu Y, Yue Z, Liu A, Yang P, Zhu M. P-type Cu-doped $Zn_{0.3}Cd_{0.7}S$/graphene photocathode for efficient water splitting in a photoelectrochemical tandem cell. ACS Sustain Chem Eng 2016;4:2569–77.
[60] Swain Gayatri, Sultana Sabiha, Naik Brundabana, Parida Kulamani. Coupling of crumpled-type novel MoS_2 with CeO_2 nanoparticles: a noble-metal-free p–n heterojunction composite for visible light photocatalytic $_H$2 production. ACS Omega 2017;2(7):3745–53.
[61] Liu Ying, Yu Yu-Xiang, Zhang Wei-De. MoS_2/CdS heterojunction with high photoelectrochemical activity for H2 evolution under visible light: the role of MoS_2. J Phys Chem C 2013;117(25):12949–57.